FtsZ treadmilling is essential for Z-ring condensation and septal constriction initiation in *Bacillus subtilis* cell division

Kevin D. Whitley[1,2+], Calum Jukes[1+], Nicholas Tregidgo[1], Eleni Karinou[1], Pedro Almada[3], Ricardo Henriques[3], Cees Dekker[2], and Séamus Holden[1*]

[1]Centre for Bacterial Cell Biology, Biosciences Institute, Faculty of Medical Sciences, Newcastle University, Newcastle upon Tyne, UK; [2]Department of Bionanoscience, Kavli Institute of Nanoscience Delft, Delft University of Technology, Delft, The Netherlands; [3]MRC-Laboratory for Molecular Cell Biology, University College London, London, UK

*Corresponding author: seamus.holden@ncl.ac.uk

+Equal author contribution

ABSTRACT

Despite the central role of division in bacterial physiology, how division proteins work together as a nanoscale machine to divide the cell remains poorly understood. Cell division by cell wall synthesis proteins is guided by the cytoskeleton protein FtsZ, which assembles at mid-cell as a dense Z-ring formed of treadmilling filaments[1,2]. However, although FtsZ treadmilling is essential for cell division, the function of FtsZ treadmilling remains unclear[2–5]. Here, we systematically resolve the function of FtsZ treadmilling across each stage of division in the Gram-positive model organism *Bacillus subtilis* using a novel combination of nanofabrication, advanced microscopy, and microfluidics to measure the division-protein dynamics in live cells with ultrahigh sensitivity. We find that FtsZ treadmilling has two essential functions: mediating condensation of diffuse FtsZ filaments into a dense Z-ring, and initiating constriction by guiding septal cell wall synthesis. After constriction initiation, FtsZ treadmilling has a dispensable function in accelerating septal constriction rate. Our results show that FtsZ treadmilling is critical for assembling and initiating the bacterial cell division machine.

INTRODUCTION

Bacterial cell division is an essential cellular process and a key target for antibiotics. Bacterial cell division is also a remarkable feat of molecular self-assembly where a nanoscale divisome machine builds a micron-scale wall (septum) at mid-cell. The core components of this machine include the septal cell-wall synthases that insert new peptidoglycan (PG) to build the septum, and the essential cytoskeletal tubulin homologue FtsZ that polymerises into a dense "Z-ring" band of short filaments at mid-cell[6–8]. These short FtsZ filaments move by treadmilling, a type of motion where an asymmetric filament undergoes plus-end polymerisation and minus-end depolymerisation, with GTP hydrolysis setting the rate of FtsZ depolymerisation and overall treadmilling speed[1,2,9]. FtsZ treadmilling dynamics are essential for cell division[2–5].

However, the role of FtsZ treadmilling in cell division remains unclear. In the Gram-positive model organism *Bacillus subtilis*, we previously observed that constriction rate and synthase speed was dependent upon FtsZ filament speed[1], leading to an initial model of a tightly coupled motile cytoskeleton-synthase complex, where FtsZ acts an obligatory guide and rate-limiting step for septal PG synthesis. In contrast, FtsZ treadmilling is dispensable after constriction initiation in *Staphylococcus aureus*[3], even though the two organisms belong to the same phylogenetic class. This could reflect genuine differences between species, or there may exist a common division mechanism where FtsZ treadmilling plays different roles at different division stages. To date, it remains unclear how the role of treadmilling FtsZ filaments varies across the full division process.

Here, we measure the dynamics and function of FtsZ treadmilling across all division stages in *B. subtilis*. To make these observations, we developed a new method combining nanofabrication, advanced microscopy, and microfluidics. This approach allowed us to measure native FtsZ dynamics at near-single-filament resolution throughout division. We found that treadmilling dynamics drive FtsZ filament interactions during Z-ring assembly and that this stabilises filaments into dense Z-rings. We determined that the FtsZ inhibitor PC190723 arrests FtsZ treadmilling within seconds, independent of division stage, allowing us to elucidate the rapid response of cells to treadmilling arrest. By systematically determining the response of single cells to FtsZ treadmilling arrest by PC190723, we found that FtsZ treadmilling has two separate essential functions: mediating Z-ring assembly during the earliest stage of cell division, and subsequently for guiding septal constriction initiation. We found that FtsZ treadmilling becomes dispensable after constriction initiation but increases septal constriction rate, reconciling the findings from previous studies[1,3]. Our results show that the key roles of FtsZ treadmilling are to drive Z-ring assembly and to initiate septal constriction.

RESULTS

FtsZ assembly at mid-cell has three distinct phases: nascent, mature, and constricting Z-rings

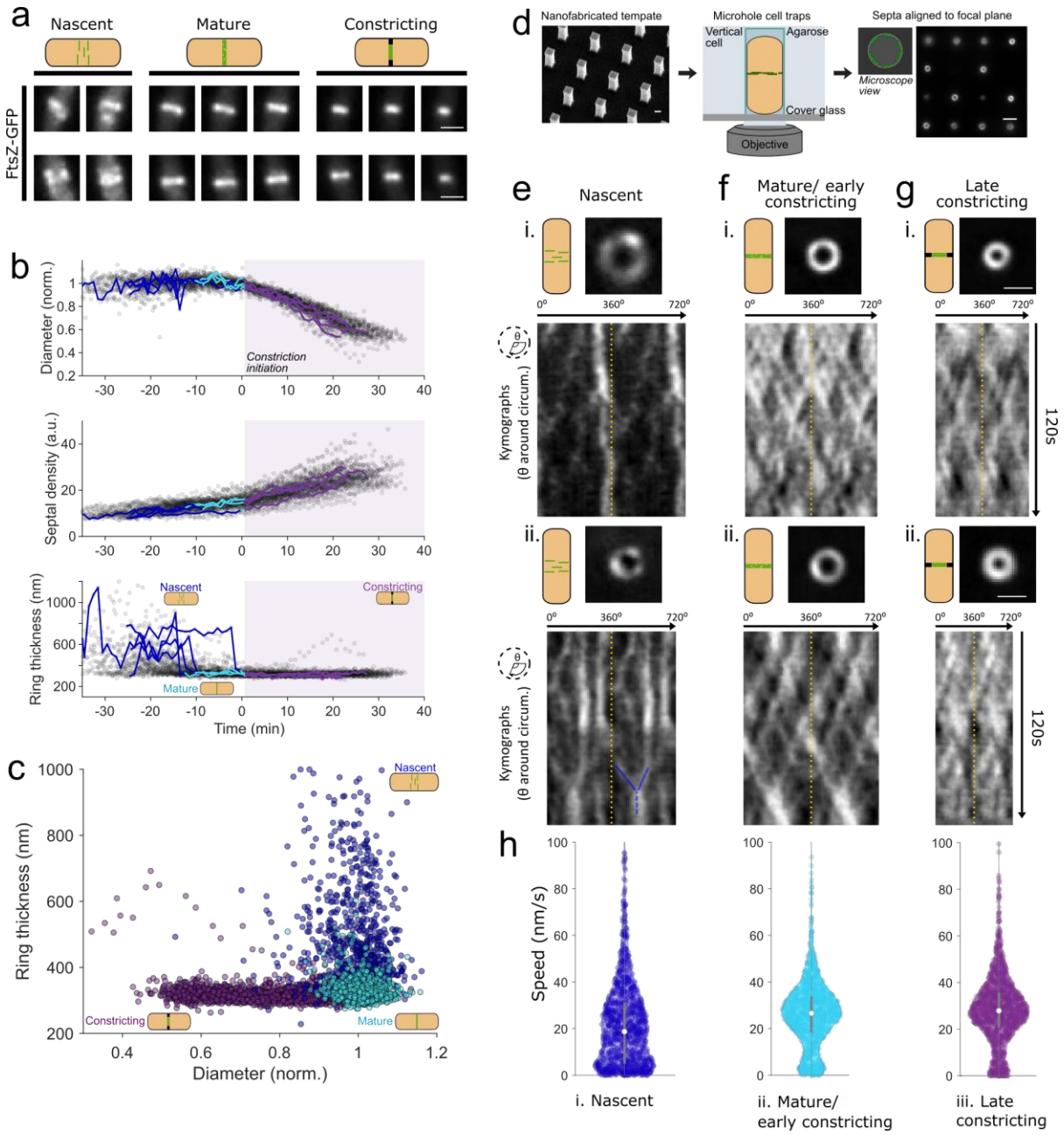

Figure 1. FtsZ filament organisation and dynamics throughout the division process. *(a) Exemplar images of FtsZ-GFP (SH130) filament organisation throughout division, classified by division phase. (b) Quantification of FtsZ-ring diameter, ring thickness and septal density (septal intensity divided by ring circumference) throughout division from time-lapse microscopy data*. Nascent Z-rings have large axial width (ring thickness) due to the diffuse distribution of filaments, which condense into a thin mature Z-ring, followed by constriction initiation. Traces are temporally aligned relative to the start time of constriction (Methods). Grey scatter points represent all data points. Lines show individual, representative traces, which are split into coloured segments indicating cell division state: nascent (blue), mature (cyan), and constricting (purple). *(c) FtsZ-ring thickness and relative septal diameter.* Colour indicates cell division state as per (b). Cell division state of FtsZ-rings in (b-c) determined by automated classification of Z-ring diameter and axial thickness time lapse data (Methods, SI Note 3). *(d) VerCINI schematic.* Rod-shaped bacteria are trapped in agarose microholes, rotating the division septum into microscope imaging plane. *(e-g) VerCINI microscopy of FtsZ filament dynamics for each Z-ring phase, two representative examples per phase (i-ii)*. Nascent Z-rings are composed of sparse filaments diffusely distributed around the circumference of the cell, and a large fraction of immobile FtsZ filaments. Mature and constricting Z-rings possess a more uniform distribution of FtsZ filaments around the division site, with most filaments treadmilling. Images of septa show the first frame in kymographs (t=0 s). Kymographs were obtained by fitting septal images to circles and plotting intensity values around the circumference of

the cell for each frame of the time-lapse (1 frame/ s). Two full revolutions around the cell (0-720°) are plotted side-by-side in each kymograph to resolve filament trajectories that pass 0°/360°, separated by yellow dotted lines. Blue lines highlight example of motile FtsZ filament aggregation. *(h) Violin plots of FtsZ filament speed for each Z-ring phase.* White circles, median; thick grey lines, interquartile range; thin grey lines, 1.5x interquartile range.

We first determined FtsZ organisation during cell division in *B. subtilis* using an FtsZ-GFP fusion[10] expressed from the native locus at wild-type protein levels (SH130, Methods, Supplementary Figure 1). Cell morphology analysis showed near native morphology at 30°C and only a mild elongation phenotype at 37°C (Supplementary Figure 2), although growth in liquid culture was not impaired at either temperature (Supplementary Figure 3).

We performed time-lapse imaging of FtsZ-GFP organisation in slow growth conditions (Figure 1; Supplementary Video 1). We observed that FtsZ filaments initially formed a diffuse structure at mid-cell which rapidly condensed into a dense narrow band, followed by the onset of constriction (Figure 1a). We quantified these changes in Z-ring structure by measuring the dimensions (thicknesses and diameters) and septal density (total septal intensity divided by Z-ring circumference) of the Z-rings in each frame (Methods). The resulting traces of thicknesses and diameters over time were aligned by the start time of constriction (Methods, Figure 1b). These time traces revealed three distinct Z-ring stages that we classified as 'nascent', 'mature', and 'constricting' based on Z-ring diameter and axial thickness (Figure 1b, Methods, Supplementary Note 3). During the nascent Z-ring stage, low density FtsZ filaments transiently assemble at mid-cell over a wide region, consistent with previous reports[4,13–15]. FtsZ filaments then rapidly condense into a thin mature Z-ring structure, which remains unconstricted but increases in intensity for some time. Finally, the Z-ring begins constricting until division is finished. Step finding analysis of Z-ring axial thickness time traces showed that Z-ring condensation occurs rapidly and stochastically approximately 10 minutes before constriction initiation (Figure 1b, Methods, Supplementary Figure 4).

VerCINI microscopy reveals FtsZ filament dynamics are division stage regulated and FtsZ treadmilling drives filament encounter in nascent Z-rings

FtsZ filament dynamics are difficult to observe *in vivo*. TIRF imaging only illuminates a thin slice of the septum, limiting observation to partial snapshots of filament dynamics in nascent Z-rings[1,2]. We previously developed a prototype approach which resolves this problem by vertically immobilizing cells in nanofabricated chambers, allowing continuous imaging of the entire division septum, including dense actively constricting Z-rings[1,4]. However, the prototype method was not capable of imaging dim, nascent Z-rings due to high background, suffered from fast photobleaching and lacked the throughput required.

We created an entirely redesigned vertical cell immobilisation method which addresses all of these issues and allows ultrasensitive high-resolution imaging of FtsZ filament dynamics at all stages of division, termed VerCINI (Vertical Cell Imaging by Nanostructured Immobilisation). This new method features a high-throughput chip design, centrifugation loading, high SNR ring-HiLO illumination[16], imaging denoising[17], and custom septal localisation and background subtraction algorithms (Methods, Supplementary Figure 5-6, Supplementary Videos 2-3). We measured FtsZ filament dynamics during each division stage using VerCINI (Figure 1e-h, Supplementary Figure 7, Supplementary Videos 4-6)[1,21]. Division stage was determined based on septal intensity and diameter (Methods, Supplementary Figure 8, Supplementary Note 3).

In nascent Z-rings, we observed that FtsZ filaments are sparsely distributed, with a mixture of treadmilling and immobile filaments (Figure 1f, Supplementary Figure 9a, 35% immobile, filament speed < 10 nm/s), leading to a low average filament speed with large spread (median 19 nm/s, interquartile range, IQR, 5-31, N=526). Surprisingly, we frequently observed two or more treadmilling

FtsZ filaments colliding, leading to aggregation and temporary arrest of both filaments (Figure 1eii, Supplementary Figure 7). FtsZ filament aggregation by lateral filament interactions is required to bundle FtsZ filaments and condense the Z-ring[22–26]. These data show that FtsZ treadmilling can drive filament aggregation by promoting the filament encounters required for lateral interactions.

Z-ring condensation led to a drop in the number of immobile FtsZ filaments in mature/early constricting Z-rings, yielding a significant increase in average filament speed with narrower speed distribution (15% immobile, median 27 nm/s, IQR 19-34, N=1053; Figure 1h). Simulations showed that changes in filament density had little effect on observed filaments speeds or observed fraction of immobile FtsZ filaments (Supplementary Figure 10). Filament speeds in late constricting Z-rings were similar to those of mature/early constricting Z-rings (13% immobile, median speed 28 nm/s, IQR 21-36, N=1677; Figure 1h). Due to the decreased immobile population, filaments in mature and constricting Z-rings traversed, on average, twice the distance around the septum of those in nascent rings (Supplementary Figure 9c).

The FtsZ filament lifetime (time bound to the septum) was similar at each stage of cell division: that is, although FtsZ filaments in the nascent stage are less dense and less motile, their bound lifetime remains similar (Supplementary Figure 9b). Furthermore, we found that treadmilling and immobile filaments displayed similar lifetimes (Supplementary Figure 11), suggesting that immobile filaments are dynamic. These results show that the fraction of treadmilling FtsZ filaments and their speeds are division stage regulated.

PC190723 arrests FtsZ treadmilling within seconds throughout division

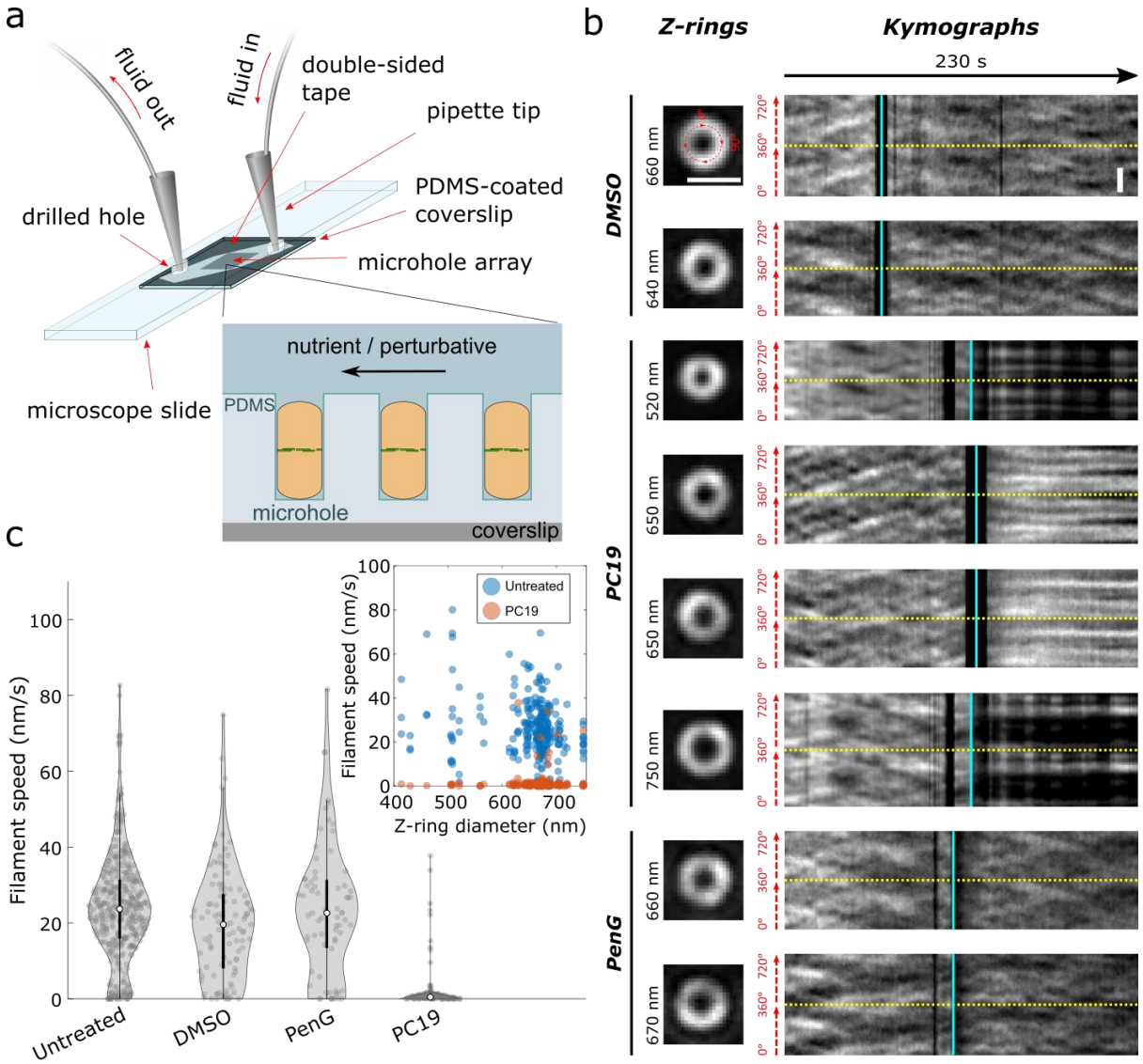

Figure 2. PC190723 arrests cellular FtsZ treadmilling within seconds across all stages of constriction. *(a) Schematic of microfluidic VerCINI.* Rod-shaped cells are confined in open-topped microholes in a thin layer of PDMS atop a microscope coverslip as solutions flow over them. The flow channel is formed from a cut piece of double-sided tape sandwiched between the PDMS layer and a microscope cover slide with drilled holes to allow inlet and outlet tubes. *(b) Representative images of septa and associated kymographs of FtsZ-GFP (SH130) dynamics in vertically-immobilised cells during rapid treatment with either DMSO (top), PC19 (middle), or PenG (bottom) at multiple septal diameters.* Images of septa show the first frame in kymographs (t=0 s). Kymographs were obtained by fitting septal images to circles and plotting intensity values around the circumference of the cell for each frame of the time-lapse (1 frame/s). Two full revolutions around the cell (0-720°) are plotted side-by-side in each kymograph to resolve filament trajectories that pass 0°/360°, separated by yellow dotted lines. Cyan lines show arrival time of media containing DMSO, PenG, or PC19. Black bands around time of treatment resulted from a loss of focus during fluid exchange. Fluctuations in intensity for two septa post-PC19 treatment (750 nm and 520 nm diameter septa) resulted from manual refocusing during imaging. Scale bars: 1000 nm. *(c) Violin plots of FtsZ treadmilling speeds pre- and post-treatment measured from kymographs.* White circles, median; thick black lines, interquartile range; thin black lines, 1.5x interquartile range. DABEST plots of effect size can be found in Supplementary Figure 12. *Inset:* FtsZ treadmilling speed distributions for untreated (white circles) and PC19-treated (red circles) cells from violin plots separated by septal diameter.

We next set out to determine the function of FtsZ treadmilling during each stage of cell division. For this we needed to observe the effect on cell division in response to rapid FtsZ treadmilling arrest. The antibiotic PC190723 (PC19) arrests FtsZ treadmilling in *B. subtilis* and related species by supporting the 'open' conformation of FtsZ and stabilizing protofilaments[1,18–21] without fully abolishing subunit turnover or GTPase activity[22]. Since the entire cell division process takes only 10-20 minutes in fast

growth conditions, it was critical to determine whether PC19 acted sufficiently rapidly and robustly for use in dissecting the effect of treadmilling during each division stage. To determine how PC19 and other cell division inhibitors perturb FtsZ treadmilling, we developed microfluidic VerCINI, which combines high-resolution imaging of cell division protein dynamics *in vivo* with rapid chemical perturbation (Methods, Figure 2a). In this method, cells are confined in an array of open-topped microholes formed from PDMS atop a microscope coverslip, which is contained within a microfluidic chamber to allow continual flow of fresh media as well as chemical inhibitors. PDMS was used rather than agarose in order to produce a thin enough layer (~50 µm) to image through. Cells continued to grow and divide, consistent with previous observations that growth of *B. subtilis* cells in sufficiently wide (>0.8 µm) PDMS channels is not impaired[23], and models demonstrating that nutrient transport does not significantly limit growth in short (<20 µm) channels[24]. A real-time image-based autofocus system was used to stabilise focus during high-speed imaging[25].

We imaged FtsZ-GFP (SH130) using microfluidic VerCINI to observe the effects of division inhibitors PC19 and Penicillin G (PenG) on FtsZ treadmilling. We recorded untreated FtsZ dynamics for 90 s while blank media flowed over the cells, then continuously treated cells with an excess of division inhibitor by changing fluid flow to media laced with the compound (Figure 2b, Supplementary Video 7). FtsZ treadmilling dynamics were abolished by PC19 within a few seconds for all diameters of septa observed (Figure 2c). When we treated cells with Penicillin G (PenG), which inhibits cell wall synthesis by binding to cell wall synthase transpeptidation sites, FtsZ dynamics continued unperturbed for the duration of the experiment (several minutes). FtsZ dynamics were also unaffected by a DMSO-only control, the solvent for PC19 (Figure 2c, Supplementary Videos 8-9).

By providing high spatiotemporal resolution during rapid chemical perturbation, microfluidic VerCINI revealed the effect of division inhibitors on FtsZ treadmilling throughout division. Our results demonstrate that PC19 inhibits FtsZ treadmilling within seconds well after the start of constriction, whereas PenG treatment does not directly affect FtsZ dynamics.

191 **FtsZ treadmilling is essential for Z-ring condensation and septal constriction initiation, but is**
192 **subsequently dispensable**

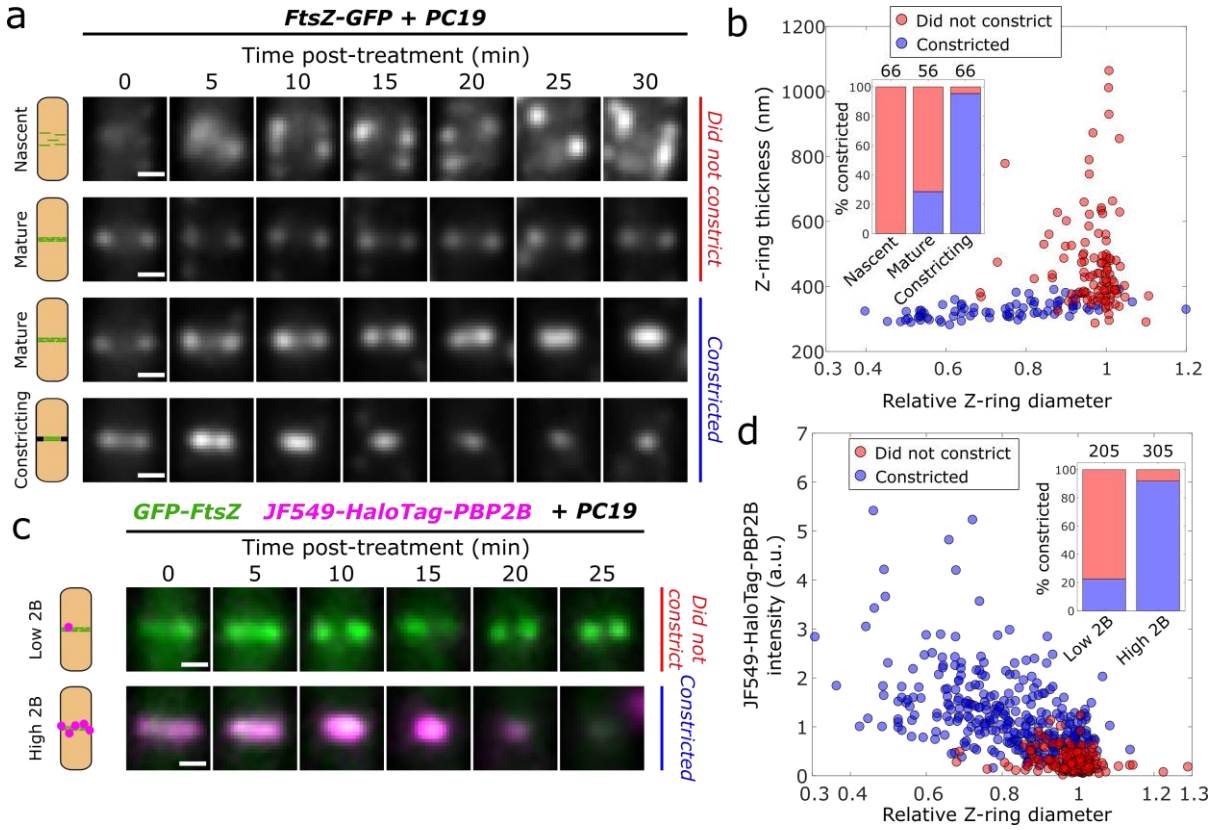

193

194 **Figure 3. FtsZ treadmilling is required until the arrival of PG synthesis machinery.** *(a) Representative time-lapses of Z-rings*
195 *for FtsZ-GFP cells (SH130) after arrival of 10 µM PC19-laced media.* Nascent rings and many mature rings do not constrict for
196 tens of minutes after PC19 treatment, whereas constricting rings and many mature rings continue constricting after
197 treatment. *(b) Scatter plot of Z-ring diameters and thicknesses for all FtsZ-GFP cells at t=0 min showing whether they*
198 *continued constricting (blue) or not (red). Inset*: Percentage of cells that continued constricting classified by division stage.
199 Nascent: thickness>400 nm, mature: thickness<400 nm, relative diameter>0.9, constricting: thickness<400 nm, relative
200 diameter<0.9. *(c) Representative time-lapses of rings from two-colour strain SH212 (Green: GFP-FtsZ, magenta: JF549-*
201 *HaloTag-PBP2B) after the arrival of PC19-laced media.* Z-rings with low HT-PBP2B signal typically do not continue constricting
202 while those with high signal typically do. *(d) Scatter plot of Z-ring diameters and normalised HT-PBP2B intensities for mature*
203 *Z-rings only at t=0 min showing whether they continued constricting (blue) or not (red). Inset:* Percentage of cells that
204 continued constricting classified by JF549-HaloTag-PBP2B signal. Low 2B: intensity<0.5, high 2B: intensity>0.5. Scale bars:
205 500 nm. Numbers above stacked bars indicate number of cells.

206 We used PC19 to investigate the role of FtsZ treadmilling throughout cell division. We imaged cells in
207 fast growth conditions (rich media, 37°C) using a commercial microfluidic device with continual fluid
208 flow both before and during treatment with excess PC19 (Figure 3, Methods). Treatment with PC19
209 prevented Z-rings in earlier stages of division from continuing to divide, but Z-rings in later stages
210 continued dividing (Figure 3a-b, Supplementary Videos 10-13). PC19 treatment prevented 96% (N=62)
211 of nascent Z-rings from condensing into mature Z-rings (Supplementary Figure 13) and 100% (N=66)
212 from constricting (Figure 3b). Furthermore, we found that treatment prevented 71% (N=56) of mature
213 Z-rings from beginning constriction, while only 5% (N=66) of initially constricting Z-rings were
214 prevented from continuing constriction. In contrast, treatment with PenG inhibited constriction
215 altogether (Supplementary Video 14). Similar results were observed in slow growth conditions (poor
216 media, 30°C; Supplementary Figure 14, Supplementary Video 15). Together these data suggest that
217 FtsZ treadmilling is required for the condensation of filaments from a nascent to a mature Z-ring, but
218 becomes dispensable at some point during the mature Z-ring stage.

219 It is worth noting that PC19 also affects FtsZ GTPase activity and filament structure[18]. These are likely
220 downstream effects of the primary mode of action, which is to stabilize the polymeric state of the
221 protein. We note that FtsZ retains ~25% GTPase activity even with excess PC19[18]. Furthermore, in cells
222 treated with 8j (a relative of PC19) the subunits in immobile FtsZ foci still turn over slowly[22], which
223 suggests filaments are still dynamic despite not treadmilling. So, while we cannot strictly rule out the
224 possibility that our observations result from a downstream effect of PC19, we believe the most
225 parsimonious explanation for our results is that the arrest of treadmilling specifically is responsible.

226 We considered whether these effects were specific to PC19 by repeating the assay with the non-
227 benzamide FtsZ inhibitor PC58538 (PC58). This compound inhibits FtsZ by a separate mode of action
228 from PC19: Rather than stabilizing protofilaments, it prevents filament assembly[26]. As with PC19, PC58
229 prevented 84% (N=50) of nascent Z-rings from condensing into mature Z-rings and 90% (N=50) from
230 constricting, but prevented 60% (N=52) of mature and only 6% (N=33) of constricting Z-rings from
231 constricting (Supplementary Figure 15, Supplementary Video 16). Interestingly, similar results were
232 recently demonstrated using ADEP antibiotics, which activate the protease ClpP to degrade FtsZ
233 monomers and thereby deplete the cytoplasmic pool needed for filament assembly[27]. We conclude
234 that arresting FtsZ treadmilling with PC19 produces an effect similar to, and as severe as, preventing
235 FtsZ filament assembly altogether, emphasizing the critical role of FtsZ treadmilling in cell division
236 initiation.

237 To further investigate the role of FtsZ treadmilling in Z-ring condensation, we examined the effect of
238 an FtsZ mutant that is deficient in GTP hydrolysis. The mutant FtsZ(D212A) in *E. coli* was shown to have
239 greatly reduced GTPase activity[28,29], and exogenous expression of the equivalent FtsZ(D213A) mutant
240 in *B. subtilis* reduces FtsZ treadmilling speed[1] (Supplementary Figure 16). We constructed a
241 merodiploid strain expressing FtsZ-GFP from the native locus and FtsZ(D213A) from a secondary locus
242 under an IPTG-inducible promoter (SH131, Methods). For comparison to wild-type (Figure 1) we
243 imaged this strain under slow growth conditions (poor media, 30°C) with an induction level (10 µM
244 IPTG) that supported growth in liquid culture (Supplementary Figure 3) and cell division
245 (Supplementary Video 17). Condensation of nascent Z-rings was significantly perturbed under these
246 conditions: 54% (N=74) of nascent Z-rings failed to fully condense prior to constriction initiation, and
247 even throughout constriction Z-rings remained 65 nm (95% CI [63,67]) thicker than wild-type
248 (Supplementary Figure 17), consistent with previous measurements in *E. coli*[30]. This partially
249 deleterious effect on Z-ring condensation is consistent with partial inhibition of FtsZ treadmilling
250 caused by expression of the GTPase-deficient mutant. Interestingly, many incompletely-condensed Z-
251 rings were still able to constrict, implying that cells can tolerate some degree of error in the
252 condensation step.

253 We next wondered what events within the mature Z-ring stage corresponded to the change in
254 dispensability of FtsZ treadmilling. Divisome assembly in *B. subtilis* is approximately a two-step process
255 where FtsZ and other cytoplasmic proteins arrive first, followed by arrival of the PG synthesis
256 machinery just before constriction initiation, including the septal transpeptidase PBP2B[31]. To
257 determine when FtsZ treadmilling becomes dispensable within mature Z-rings, we repeated the
258 treadmilling inhibition assay using a 2-colour strain where FtsZ and PBP2B are both labelled. Since
259 fully-labelled FtsZ slightly perturbed cell physiology (Supplementary Figure 2) and full labelling of FtsZ
260 was unnecessary for this assay, for the labelled FtsZ we decided to use a well-characterized
261 merodiploid harbouring an N-terminal GFP-FtsZ fusion[22] that could be expressed at a low non-
262 perturbative level. We therefore constructed a 2-colour strain (SH212, Methods) expressing GFP-FtsZ
263 from an ectopic locus and HaloTag-PBP2B from its native locus. To quantify the amount of PBP2B at
264 septa, we labelled HaloTag-PBP2B with an excess of JF549 HaloTag ligand[32] (Methods). This strain
265 showed the same response overall to PC19 treatment as before (Supplementary Figure 18,

266 Supplementary Videos 18-19). For mature rings we found that the amount of PBP2B present at time
267 of FtsZ treadmilling arrest correlated strongly with whether rings would constrict or not (Figure 3c-d).
268 Similar results were obtained for a functional mNeonGreen-PBP2B fusion expressed from the native
269 locus[1] (ME7 Supplementary Video 20, Supplementary Figure 19). The GFP-FtsZ signal also increased
270 during the mature ring stage, but unlike PBP2B the FtsZ signal was only weakly correlated with the
271 percentage of cells continuing constriction (Supplementary Figure 18b). FtsZ treadmilling thus
272 becomes dispensable for cell division just after the arrival of the PG synthesis machinery. These results
273 are consistent with previous findings in *S. aureus* that FtsZ treadmilling is required until constriction
274 has initiated, and thereafter becomes dispensable[3]. Since we previously observed that FtsZ
275 treadmilling guides processive PG synthesis around the septum[1], we conclude that FtsZ treadmilling
276 in mature Z-rings likely functions by guiding the processive motion of septal synthases during the
277 earliest stages of septal synthesis, before a septum has been formed.

278 Together, our data reveal two essential functions for FtsZ treadmilling in division. The first is a novel
279 peptidoglycan synthesis-independent function, to condense sparse FtsZ filaments into a dense Z-ring.
280 The second function is to initiate constriction by guiding initial cell-wall synthesis.

281 **FtsZ treadmilling accelerates constriction**

282 We wondered how to reconcile the finding that FtsZ treadmilling is dispensable for constriction after
283 initiation, with our previous observation that FtsZ treadmilling sets the rate of constriction[1]. To
284 address this, we set out to determine the effect of rapid, total arrest of FtsZ treadmilling on the septal
285 constriction rate. In order to precisely measure constriction rates immediately after PC19 treatment,
286 we developed a physical model for Gram-positive septal constriction which could be fitted to partial
287 septal constriction trajectories immediately after cell treatment with PC19 (Methods, Supplementary
288 Note 2, Figure 4a). For comparison to previous observations we converted the observed constriction
289 rates of partially constricted cells to an effective constriction time t_{eff}, the total amount of time it would
290 take for an average septum to constrict completely (Methods).

291 We observed that the constriction time of untreated cells in fast growth conditions was 15.3 min, IQR
292 13.5-17.9 (N=765, Figure 4b). FtsZ treadmilling inhibition by PC19 treatment caused a robust 7.7 min,
293 95% CI [6.9,8.3] (N=419), increase in constriction time for cells grown in rich media. This is similar to
294 the increase in constriction time caused by high expression of the GTP-hydrolysis-impaired
295 FtsZ(D213A) mutant (Supplementary Figure 20). Fluorescent PBP2B signal continued to increase after
296 treatment with PC19 (Supplementary Figure 21), indicating that the reduced constriction rate is
297 unlikely to be caused by indirect reduction of synthase levels at the septum. These results show that
298 although FtsZ treadmilling is not required for septal PG synthesis after constriction initiation,
299 treadmilling promotes efficient constriction by increasing septal constriction rate. This reconciles
300 apparently contradictory models previously proposed for the role of FtsZ treadmilling in septal
301 constriction[1,3].

302

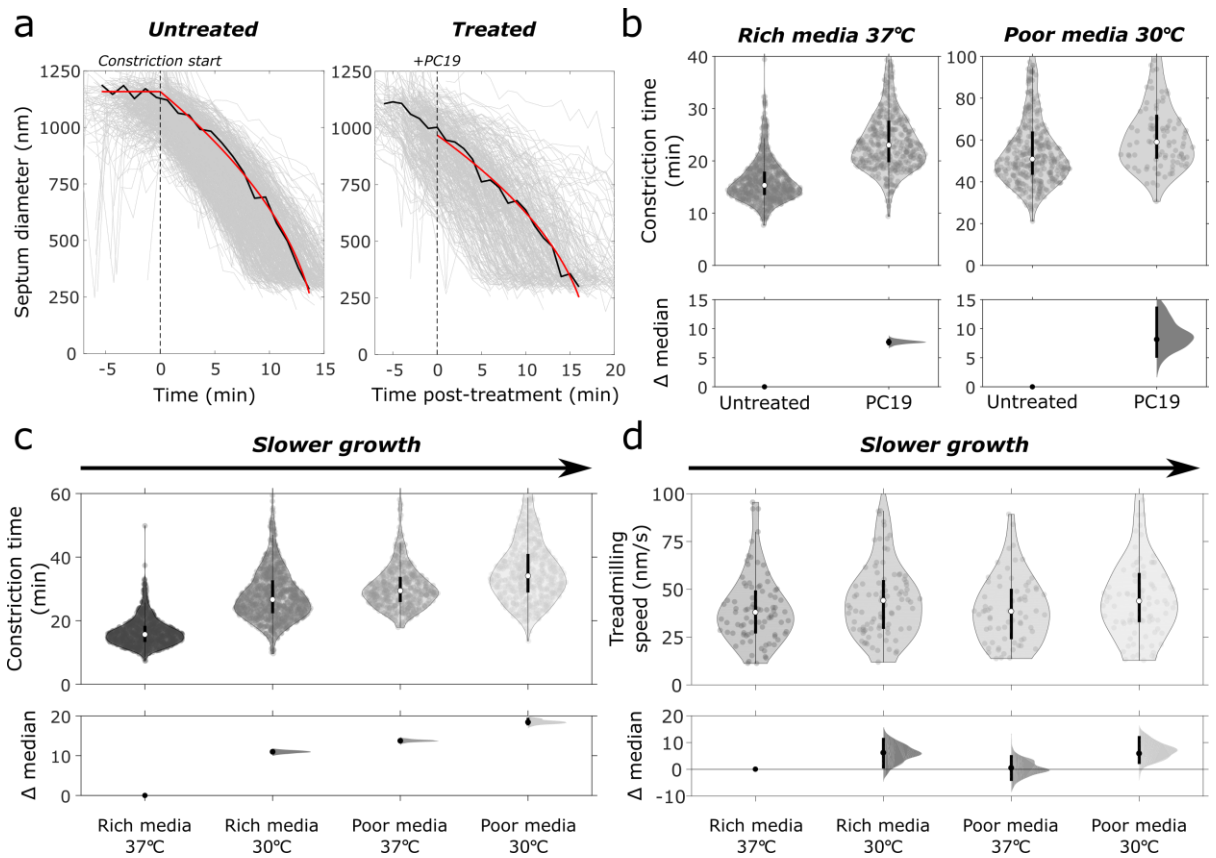

Figure 4. Constriction rate is accelerated by FtsZ treadmilling and fast cell growth rate. *(a) Time traces of ring diameters from mNeonGreen-PBP2B strain (ME7) for untreated (left) and PC19-treated (right) cells with constant PG synthesis model (red) fitted to representative traces (black).* Untreated cell trajectories are aligned relative to fitted constriction start time. PC19-treated cell trajectories are aligned relative to the arrival time of PC19-laced media. *(b) Constriction time before and after PC19 treatment for both fast growth (rich media 37°C) and slow growth (poor media, 30°C) conditions. (c) Constriction time of mNeonGreen-PBP2B cells in rich and poor media at two growth temperatures. (d) FtsZ-mNeonGreen (bWM4) treadmilling speeds in different media and temperature. Top panels, b-d:* violin plots; white circle, sample median; thick black lines, interquartile range; thin black lines, 1.5x interquartile range. *Bottom panels, b-d: Bottom panels:* DABEST plots showing effect size analysis, compared to leftmost condition; black circles, median difference; error bars, 95% confidence interval of median difference.

Cell growth rate limits septal constriction rate independently of FtsZ treadmilling

Growth rate and cell size for most bacterial species are linked to nutrient availability and culture temperature[33]. We sought to identify how growth rate affects the constriction rate of *B. subtilis* cells. We measured the constriction rate in media and temperature conditions (Supplementary Figure 3c; Supplementary Table 1) using a strain expressing PBP2B from its native promoter fused to mNeonGreen (ME7, Methods). Slower growth in either minimal media or at low temperature led to correspondingly longer constriction times (Figure 4a, Supplementary Figure 3d), with a 2.18-fold (95% CI [2.12,2.24]) difference in constriction time between fastest and slowest growth conditions. We determined FtsZ treadmilling speed for all conditions using a dilute exogenous label of FtsZ-mNeonGreen (bWM4) which shows no growth or morphology phenotype at 37°C[1]. FtsZ treadmilling speed was constant across all growth conditions tested (Figure 4b), showing that the effect of growth rate on septal constriction is independent of FtsZ treadmilling.

We next investigated whether FtsZ treadmilling also promotes constriction in slow growth conditions. As in fast growth conditions, arresting FtsZ treadmilling increased the constriction time (Figure 4b, Supplementary Video 21). However, the relative increase in constriction time was much lower in slow growth conditions (1.16-fold 95% CI [1.09,1.24] vs 1.50-fold 95% CI [1.46,1.55] change). These

330 observations show that cell growth rate is a major regulator of active septal constriction, with
331 treadmilling FtsZ filaments acting as a secondary promotor of septal synthesis.

332 **DISCUSSION**

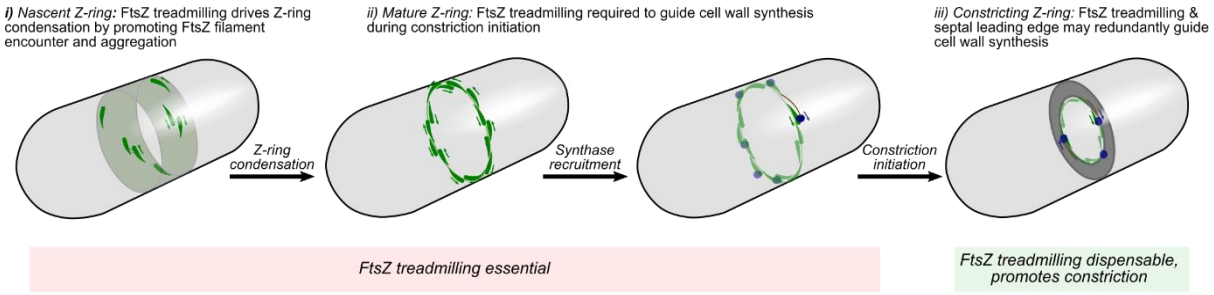

333
334 **Figure 5: Model for function of FtsZ treadmilling in Z-ring assembly and septal constriction.**

335 Using bespoke ultra-sensitive microscopy of cell division protein dynamics, we discovered that FtsZ
336 treadmilling plays two separate essential roles in cell division: to establish the mature divisome by
337 condensing diffuse filaments into a dense ring, and to guide septal constriction initiation (Figure 5).

338 We found that condensation of sparse FtsZ filaments into a dense Z-ring is required for cell division.
339 Using VerCINI microscopy we observed that treadmilling FtsZ filaments frequently collide and
340 aggregate in nascent Z-rings. We also found that nascent Z-rings contain a large fraction of immobile
341 FtsZ filaments, which do not treadmill, and that Z-ring condensation promotes formation of
342 treadmilling FtsZ filaments. While the mechanism of FtsZ filament motility regulation requires further
343 study, *in vitro* measurements of FtsZ dynamics suggest that immobile FtsZ filaments could result from
344 low septal FtsZ concentration or regulation by accessory/anchor proteins[9].

345 Chemical arrest of treadmilling completely abolished FtsZ ring condensation. Attractive lateral
346 interactions between FtsZ filaments, via the FtsZ C-terminal-linker and cytoplasmic FtsZ-associated
347 proteins are known to mediate FtsZ bundling and Z-ring condensation[34–38]. Our results reveal an
348 additional key factor in assembling the Z-ring: FtsZ filament treadmilling drives filament interactions
349 by enabling FtsZ filaments to rapidly search the mid-cell surface circumferentially and efficiently
350 encounter one another. This finding contrasts with previous models of Z-ring condensation involving
351 lateral sliding of filaments[13,14]. We conclude that FtsZ treadmilling—likely along with FtsZ lateral
352 interactions—drives aggregation of FtsZ filaments into a condensed Z-ring. This is remarkably
353 reminiscent of treadmilling-driven partitioning of FtsZ filaments into higher-order structures
354 previously observed *in vitro*[9,39].

355 The second role of FtsZ treadmilling is to guide septal PG synthesis. We found that this role is essential
356 in the constriction initiation phase of *B. subtilis* cell division, but dispensable afterwards. Together with
357 our previous observations that FtsZ treadmilling guides individual synthase molecules during PG
358 synthesis[1], it is likely that during constriction initiation FtsZ filament treadmilling is required to guide
359 the synthases around the circumference of the mid-cell in the absence of an established septum. We
360 also observed that FtsZ treadmilling dynamics are division stage regulated, with Z-ring condensation
361 promoting efficient FtsZ treadmilling. In addition to concentrating the division machinery into a small
362 area, Z-ring condensation may indirectly promote efficient constriction initiation by increasing the
363 fraction of treadmilling filaments available to guide cell-wall synthesis.

364 Although FtsZ treadmilling is dispensable after constriction initiation, we found that treadmilling
365 increases the rate of septal constriction by up to 1.5-fold. However, we found that overall cell growth
366 rate has a much stronger effect on septal constriction rate than FtsZ treadmilling, increasing

367 constriction rate up to 2.2-fold between fast and slow growth conditions. We conclude that FtsZ
368 treadmilling plays only a secondary role in active constriction, while its critical roles occur prior to
369 constriction initiation. This contrasts with the previous model of *B. subtilis* FtsZ as an obligatory guide
370 and rate-determining factor for constriction[1]. After constriction initiation, the highly ordered septal
371 leading edge[40] may be sufficient to act as a guide for processive septal PG synthesis, with FtsZ filaments
372 acting as a mid-cell localiser and redundant guide during active constriction.

373 The VerCINI method presented here is a powerful tool for ultra-sensitive measurement of cell division
374 protein dynamics and mode of action of cell division targeting antibiotics. We anticipate that many
375 other bacterial structures, especially the bacterial cell envelope and associated proteins, could also
376 benefit from VerCINI's high resolution top-down cell view.

377 A key puzzle in bacterial cell biology is how nanoscale division proteins spontaneously and accurately
378 build a micron-size wall at mid-cell. Treadmilling gives FtsZ filaments the remarkable ability to
379 autonomously drive their own circumferential motion around the mid-cell surface. Our results show
380 that the self-driving capability of FtsZ filaments is crucial to solving the scale problem of cell division
381 by directing divisome assembly and initial septal synthesis to a narrow band around the mid-cell, laying
382 the template for septum construction. Dynamic, self-organizing FtsZ filaments thus provide long-
383 distance order and collective motion around the bacterial mid-cell in the absence of cytoskeletal
384 motor proteins.

385 **ACKNOWLEDGEMENTS**

386 We thank Henrik Strahl (Newcastle) for helpful discussions, Ling Wu and Jeff Errington (Newcastle) for
387 strains and antibodies, Luke Lavis (HHMI) for Janelia Fluor dyes, and Ethan Garner (Harvard) for strains.
388 SH, KW, CJ and EK acknowledge funding support by a Newcastle University Research Fellowship and a
389 Wellcome Trust & Royal Society Sir Henry Dale Fellowship grant number 206670/Z/17/Z. NT supported
390 by a UK Engineering and Physical Sciences Research Council doctoral studentship. RH and PA funded
391 by grants from the UK Biotechnology and Biological Sciences Research Council (BB/M022374/1), the
392 UK Medical Research Council (MR/K015826/1), and Wellcome Trust (203276/Z/16/Z). CD and KW
393 acknowledge funding support by ERC grant SynDiv (669598) and the Netherlands Organisation for
394 Scientific Research (NWO/OCW) as part of the Frontiers of Nanoscience and Basyc programs.

395 **AUTHOR CONTRIBUTIONS**

396 KW, CJ and NT acquired data. KW, CJ, NT and SH analysed data. KW, CJ, SH and CD developed the
397 VerCINI method. KW performed nanofabrication, supervised by CD. SH, KW, PA and RH wrote
398 software. CJ, EK, NT created and characterised bacterial strains. SH and CD directed the research. KW,
399 SH and CJ wrote the manuscript with input from all authors.

400

401 ## MATERIALS AND METHODS

402 **Bacterial strains and growth conditions**

403 Strains used in this study are listed in Supplementary Table 2. Strains were streaked from -80°C freezer
404 glycerol stocks onto Nutrient Agar (NA) plates containing the relevant antibiotics and/or inducers and
405 grown overnight at 37°C. Single colonies were transferred to liquid starter cultures in either Time-
406 Lapse Medium (TLM[42]) or PHMM media and grown with agitation at 200 rpm overnight at either 30°C
407 (TLM) or 22°C (PHMM[1]). The next day, TLM starter cultures were diluted to a starting OD_{600} of 0.1 in
408 Chemically-Defined Medium (CDM[42]), while PHMM starter cultures were diluted to a starting OD_{600} of
409 0.05 in PHMM, and these liquid cultures were grown at 30°C or 37°C with any required inducer until
410 they reached the appropriate OD_{600}. When necessary, antibiotics and inducers were used at the
411 following final concentrations: chloramphenicol 5 µg/ml, spectinomycin 60 µg/ml, erythromycin
412 1 µg/ml, lincomycin 10 µg/ml, kanamycin 5 µg/ml, xylose 0.08% and IPTG 20 µM.

413 **Strain construction**

414 **SH211** (PY79 Δ*hag*) was constructed by transforming competent PY79 with genomic DNA extracted
415 from strain PB5250, using standard protocols[43]. The antibiotic resistance cassette was removed using
416 pDR224 as described previously[44].

417 **SH130** (PY79 Δ*hag ftsZ::ftsZ-gfp-cam*) was constructed by transforming SH211 competent cells with
418 genomic DNA extracted from strain PL642.

419 **SH131** (PY79 Δ*hag ftsZ::ftsZ-gfp-cam* Ω *amyE::erm*-$P_{hyperspank}$-*ftsAZ*(D213A)) was constructed by
420 transforming competent SH130 cells with genomic DNA extracted from strain bAB215.

421 **SH132** (PY79 *pbp2B::mNeonGreen-15aa-pbp2B* Ω *amyE::erm*-Phyperspank-*ftsAZ*(D213A)) was
422 constructed by transforming competent ME7 cells with genomic DNA extracted from strain bAB215.

423 **SH212** (PY79 *pbp2B::erm*-$P_{hyperspank}$-*HaloTag-15aa-pbp2B* Ω *amyE::spc* P_{xyl} *gfp-ftsZ*) was constructed by
424 transforming competent bGS28 cells with genomic DNA extracted from strain 2020. All published
425 strains are available on request to the authors.

426 **Bacterial strain characterization**

427 Strains were characterised by growth in liquid culture (Supplementary Figure 3) and cell morphology
428 analysis (Supplementary Figure 2). Fluorescent fusion protein levels for relevant strains were
429 determined by Western blotting (Supplementary Figure 1).

430 **Growth curves**

431 *B. subtilis* PY79 and variant strains were grown overnight in TLM or PHMM containing the relevant
432 inducers. Overnight cells were diluted to an OD_{600} of 0.05 in either CDM or PHMM, respectively, and
433 200 µL were used in a 96-well microtiter plate. Growth was monitored for 12 hours using a FluoStar
434 plate reader (BMG Labtech).

435 **Cell morphology analysis**

436 PY79 and SH130 cultures were prepared for imaging in CDM or PHMM as described above. Once the
437 cultures had reached OD_{600} 0.4-0.5, Nile Red was added to 200 µl of cells to a working concentration
438 of 1 µg/ml, and incubated at growth temperatures for 5 mins, prepared on agarose microscope slides
439 as described below and cell morphology images recorded. Cell length was then manually determined
440 using ImageJ.

441 **Western blotting**

442 Overnight cultures of specified strains were grown overnight in LB at 30°C. The following morning,
443 cultures were diluted to ~OD_{600} 0.05 and grown at 30°C until ~OD_{600} 0.6. Cells were harvested by
444 centrifugation and stored at 20°C for further processing. Samples were normalised based on OD600,
445 re-suspended in 2x SDS protein sample buffer and heated at 80°C for 10 minutes followed by
446 centrifugation.20 µL lysates were then separated by SDS PAGE in 10% polyacrylamide gel.. FtsZ and
447 PBP2B were detected using a FtsZ polyclonal (Sigma, 1:10000 dilution) and a PBP2B polyclonal (Merck,
448 1:5000 dilution) antibody, respectively, followed by a HRP-conjugated anti-rabbit IgG antibody
449 (Sigma). Samples were developed using Pierce™ ECL Western Blotting Substrate (Thermofisher) and
450 imaged using an ImageQuant LAS 4000 mini Biomolecular Imager (GE Healthcare).

451 **Microscopy**

452 Power density, exposure time and other key parameters are listed for each microscopy experiment in
453 Supplementary Table 4. All imaging was done using either a Nikon N-SIM/N-STORM inverted
454 fluorescence microscope (Figure 4, Supplementary Figure 22) or a custom-built inverted microscope
455 (otherwise).

456 *Nikon N-STORM.* Cells were illuminated with a 488 nm line from an Argon Ion laser (CVI Melles-Griot).
457 A 100x TIRF objective (Nikon CFI Apochromat TIRF 100XC Oil) was used for imaging and an Andor iXon
458 DU897 EMCCD camera was used, with a 1.5x OptoVar (Nikon) and standard Nikon tube lens, giving an
459 effective image pixel size of 106 nm/pixel. Cells were illuminated via HiLO[45] inclined illumination to
460 minimise background using an objective TIRF module (Nikon N-STORM module) using 488 nm laser
461 excitation.

462 *Custom microscope.* Cells were illuminated with a 488 nm laser (Obis) and/or a 561 nm laser (Obis) as
463 indicated. A 100x TIRF objective (Nikon CFI Apochromat TIRF 100XC Oil) was used for all experiments
464 except microfluidic VerCINI measurements where a 100x silicone immersion objective (CFI SR HP Plan
465 Apochromat Lambda S 100XC Sil, Nikon) was used for deep focusing. A 200 mm tube lens (Thorlabs
466 TTL200) and Prime BSI sCMOS camera (Teledyne Photometrics) were used for imaging, giving effective
467 image pixel size of 65 nm/pixel. Imaging was done with a custom-built ring-TIRF module operated in
468 ring-HiLO[45] using a pair of galvanometer mirrors (Thorlabs) spinning at 200 Hz to provide uniform, high
469 SNR illumination.

470 **Nanofabrication**

471 Micropillars were patterned using electron-beam lithography and etched using reactive-ion etching.
472 Briefly, a silicon wafer was spin coated with AR-N 7700.18 (Allresist GmbH). Features were patterned
473 using a Leica EBPG 5000+ with 56 nm beam step size. The unexposed resist was removed with solvent
474 Microposit MF-321 and the exposed wafer surface was etched using an AMS Bosch etcher. The
475 remaining resist was removed using oxygen plasma. Pillars widths ranged from 1.0 to 13 µm with
476 height 6.7 µm, spaced 5 µm apart. Final micropillar dimensions were confirmed using SEM.

477 Micropillar wafers were silanised to allow cured polydimethylsiloxane (PDMS) to be removed without
478 damaging structures. To do this, wafers were coated with (tridecafluoro-1,1,2,2-tetrahydrooctyl)
479 trichlorosilane (abcr GmbH) by vapour deposition.

480 **VerCINI**

481 Agarose microholes were formed by pouring molten 6% agarose onto the silicon micropillar array.
482 Patterned agarose was transferred into a Geneframe (Thermo Scientific) mounted on a glass slide, and
483 excess agarose was cut away to ensure sufficient oxygen. Cells at $OD_{600} \sim 0.4$ were concentrated 100x
484 by centrifugation and added onto the agarose pad. Cells were then loaded into the microholes by

485 centrifuging the mounted agarose pad with concentrated cell culture in an Eppendorf 5810 centrifuge
486 with MTP/Flex buckets. Unloaded cells were rinsed off with excess media.

487 FtsZ treadmilling dynamics were imaged at 1 frame/s (continuous exposure) for 2 mins at 1-8 W/cm^2.
488 After each field of view was imaged, a multi-slice Z-stack was taken at 500 nm intervals to exclude
489 tilted or improperly trapped cells, in addition to excluding Z-rings that have an adjacent Z-ring 1 µm
490 above or below the imaging plane. VerCINI experiments were performed on cells in a *Δhag* mutant
491 background, preventing undesirable cell rotation within the microholes by disabling flagellar motility.

492 **Microfluidic VerCINI**

493 *Device assembly*

494 Open-topped microhole coverslips were formed from PDMS using the silicon micropillar array
495 (Supplementary Figure 23). All PDMS reagents and processing equipment were from BlackHoleLab.
496 PDMS elastomer base and curing agent were mixed in a 1:1 ratio and degassed. The degassed mixture
497 was then poured on top of the microhole array and a microscope coverslip was pressed down to form
498 a thin layer. PDMS was cured by baking at 80°C for 1 hr, and the coverslip with patterned PDMS layer
499 was removed from the silicon mould.

500 Microfluidic chambers were prepared using readily-available components (Supplementary Figure 23).
501 First, holes were drilled into a glass microscope cover slide using a diamond drill bit (Kingsley North).
502 A flow channel was then made by cutting a strip of double-sided tape using either a scalpel or laser
503 engraver. One side of the double-sided tape was then adhered to the microscope cover slide. Cut
504 pipette tips were then inserted into the drilled holes, and polyethylene tubing (Smiths Medical) was
505 inserted into them. Leakage was prevented by sealing pipette tips and tubing using epoxy.

506 To load cells into the microholes, PDMS was first rendered hydrophilic by treating with air plasma for
507 3 min. A 9 mm diameter silicone gasket (Grace Bio-Labs) was then placed over the PDMS microholes.
508 Cells at $OD_{600} \sim 0.4$ were concentrated 100x by centrifugation and pipetted into the silicone gasket.
509 Cells were then loaded into the microholes by centrifuging the microhole-containing coverslip with
510 concentrated cell culture in an Eppendorf 5810 centrifuge with MTP/Flex buckets. The coverslip was
511 covered during centrifugation to prevent evaporation. Unloaded cells were rinsed off with excess
512 media. To ensure adequate loading, this loading-and-rinsing protocol was then repeated.

513 After cells were loaded into microholes, the silicone gasket was removed and the flow chamber was
514 fully assembled by adhering the PDMS-covered coverslip to the exposed side of double-sided tape on
515 the glass cover slide (Supplementary Figure 23).

516 *Imaging*

517 Due to the relatively thick (~50 µm) layer of PDMS between the coverslip surface and the confined
518 cells, a Nikon silicone immersion objective (CFI SR HP Plan Apochromat Lambda S 100XC Sil, Nikon)
519 was used for imaging due to its high working distance (0.3 mm).

520 Since the indices of refraction for PDMS and aqueous solution are similar, autofocusing systems relying
521 on the reflection of an IR signal from two interfaces were not adequate due to weak signal. Instead,
522 autofocusing was done using an image-based approach first described by McGorty and co-workers[25]
523 using cross-correlation of brightfield images. Briefly, a separate brightfield imaging pathway was
524 added to the microscope using a 1050 nm IR LED (Thorlabs) and IR-sensitive camera (UI-1220LE-M-GL,
525 Imaging Development Systems GmbH), and a plugin for Micro-Manager was developed to calculate
526 cross-correlations and move the sample stage (https://github.com/HoldenLab/DeepAutoFocus). At
527 the start of an experiment, a z-stack of IR brightfield images was obtained as a reference. During the

experiment, the cross-correlation map between every new IR brightfield image and this reference stack was calculated, and the sample stage was moved to compensate for any drift. To our knowledge this is the first application of IR cross-correlation autofocusing to live cell imaging.

Fluid control

Media was flowed through the chamber by a syringe pump (Aladdin-220, World Precision Instruments). To prevent potential leakage, media was pulled through the chamber from fluid reservoirs by operating the syringe pump in withdraw mode. Complete solution exchange occurred within 7 s of initial compound arrival time, estimated using a rhodamine tracer.

CellASIC experiments

The microfluidic CellASIC system (EMD Millipore) was used to image constricting cells during treatment with division inhibitors. Cells were loaded into B04A plates and equilibrated in blank media for ~15 min with a pressure of 2 psi (~6 µL/hr flow rate) prior to imaging.

In a typical experiment, untreated constricting cells were imaged for 30 min (1 min/frame, 1 s exposure, 1-2 W/cm^2) while blank media was flowed using 2 psi. Solution exchange was done by first flowing media with compound using 8 psi (~34 µL/hr flow rate) for 15 s, then dropping the pressure to 2 psi for the remainder of the experiment (50-90 min). DMSO treatment alone caused a small but robust increase in constriction time (Supplementary Figure 24). However, pre-adaptation of cells to blank media containing DMSO eliminated this effect, showing that observed effects of PC19 treatment resulted from the drug and not the solvent that accompanied it (Supplementary Figure 24).

The arrival time of the compound at the cells was most estimated by treating the FtsZ-GFP strain with 10 µM PC19 using our standard flow protocol. PC19 causes the diffuse cytoplasmic FtsZ-GFP to rapidly polymerise into short filaments throughout the cell (Supplementary Videos 10-13), providing a clear signal for compound arrival. From these experiments we determined that compound arrives 3-4 min after fluid exchange.

Microscopy of horizontal cells

Sample preparation

Coverslips were first cleaned by treating with air plasma for 5 min. Slides were prepared as described previously[42]: Flat 2% agarose pads of either CDM or PHMM were prepared inside Geneframes (Thermo Scientific) and cut down to strips of 5 mm width to ensure sufficient oxygen supply to cells. Cell cultures were grown to OD_{600} between 0.2 and 0.4, when 0.5 µL of cell culture was spotted on the pad. Cells were allowed to adsorb to the pad for 30 s before a plasma-cleaned coverslip was placed on them. After spotting on agarose pads, cells were allowed to equilibrate within the microscope body for 15 min before being imaged. Cells were then imaged either by TIRF microscopy for observation of FtsZ filament dynamics, or ring-HiLO for time-lapse observation, with experimental parameters defined in Supplementary Table 4.

HaloTag labelling with JF549 dye

Full labelling of HaloTag-PBP2B was done by incubating strain SH212 with 50 nM JF549 HaloTag ligand for 15 min. Cells were washed once with fresh media before imaging. JF549 HaloTag ligand was a gift from Luke Lavis[32].

Image analysis

VerCINI data analysis

569 *Pre-processing*

570 Videos were denoised using the ImageJ plugin PureDenoise[17], which is based on wavelet
571 decomposition. Key assumptions of the method are (i) local spatiotemporal similarity within the
572 image (ii) absence of sharp discontinuities, guaranteed by diffraction-limited nature of the image. The
573 denoising algorithm makes does not make any assumptions on the type of underlying biological
574 structure.

575 Denoised videos were registered using the ImageJ plugin StackReg[46]. Image stacks of vertically
576 immobilised cells were inspected to exclude tilted cells or out of focus FtsZ-rings, or FtsZ rings where
577 a second Z-ring was closer than 1 um to the focal plane. Cropped region of interest movies containing
578 single in-focus cells were manually selected and exported for analysis. An ImageJ package for VerCINI
579 data processing is available (https://github.com/HoldenLab/Ring_Analysis_IJ).

580 *VerCINI background subtraction, kymograph extraction, quantification*

581 Custom software for quantitative cytoplasmic background subtraction and kymograph extraction was
582 developed for analysis of VerCINI movies (https://github.com/HoldenLab/ring-fitting2). Fluorescence
583 images of isolated vertical cells were fitted to a joint explicit model for diffuse out-of-focus cytoplasmic
584 background (Gaussian + Cauchy model) plus septal protein signal, modelled as a 12 sectored annulus
585 with each sector of variable amplitude.

586 $$F(x,y) = Signal(x,y) + Bg(x,y)$$

587 Signal is calculated in polar coordinates, around the septal ring centre fit parameter (x_0, y_0), and then
588 transformed into Cartesian coordinates. Signal is defined as

589 $$S(r,\theta) = A_i(\theta)\exp\left(-\frac{(r-R_0)^2}{2\sigma^2}\right),$$

590 where $A_i(\theta)$ defines a 12 sectored ring. Background is defined as

591 $$Bg(x,y) = a\exp\left(\frac{-((x-x_0)^2+(y-y_0)^2)}{2\sigma_{bg1}^2}\right) + b\frac{\sigma_{bg2}^2}{(x-x_0)^2+(y-y_0)^2+\sigma_{bg2}^2} + c.$$

592 This explicit model allowed accurate sub-pixel location of a circular line profile at the septal leading
593 edge. Explicit subtraction of complex background signal also allowed septal intensity quantification.
594 The background subtracted intensity along the circular line profile was then calculated for each frame
595 and automatically plotted as a kymograph. Kymographs were plotted over the [0,720°] ie two
596 complete revolutions around the line profile for ease of visualization, specifically to allow
597 straightforward visualization of treadmilling filaments crossing the 360°,0° boundary. For each cell,
598 the Z-ring diameter was determined from the fitted model in the kymograph extraction step. Median
599 septal intensity was calculated as the median value of all kymograph pixels from the first 60 image
600 frames.

601 *FtsZ filament treadmilling analysis using VerCINI*

602 We found that automated methods for in vitro FtsZ filament speed measurements, either after Dos
603 Santos Caldas and coworkers[47] or using a similar in-house algorithm, are currently insufficient for FtsZ
604 filament speed analysis in either horizontal or vertical cells compared to manual analysis, because at
605 cellular filament density they currently perform poorly at detecting immobile filaments, break the
606 complete trajectories of treadmilling filaments into multiple shorter trajectories, and cannot reliably
607 process images from dense Z-rings in horizontal cells.

608 We therefore performed manual measurement of filament speed and processivity by kymograph
609 analysis, annotating filaments as lines in ImageJ and then measuring the angle via ImageJ script. As
610 the intensity range across kymographs is large, manual detection and analysis of filaments was aided
611 by applying a ridge filter[48] to the kymograph which detects ridges in the image, independent of
612 absolute intensity. The ridge filter consists of a Gaussian blur operation to set the feature scale and
613 suppress noise (here 2 pixels, 130 nm), followed by calculation of the major eigenvalue of the Hessian
614 matrix for each pixel, implemented as an ImageJ macro in the package listed above. Joint annotation
615 of the ridge filtered and raw intensity kymograph was performed, allowing sensitive annotation of
616 both bright and dim filaments (Supplementary Figure 25).

617 ***Horizontal cell image analysis***

618 *Pre-processing*

619 Images were denoised and registered as described above.

620 *Cell segmentation and tracking of division protein localization*

621 MicrobeJ[11] was used to track individual FtsZ-/PBP2B-rings and export their centroid coordinates for
622 analysis. To do this, image backgrounds were first subtracted using a sliding paraboloid window of 50
623 pixels and all frames were converted to 8-bit for easier thresholding.

624 Two approaches were used to identify division protein localization, depending on the experiment. For
625 measurements of septal constriction rate only (Figure 4a), which requires only detection of bright
626 dense FtsZ/PBP2B rings, a simple approach of intensity-based threshold detection was applied in
627 MicrobeJ a threshold was selected manually for each field of view using MinError. Additional area and
628 length thresholds (Area: [0.08 Inf] μm^2, Length: [0.02 1.8] µm) were established to exclude objects in
629 fields of view that were not rings. Tracks shorter than 7 frames were excluded. Data was then exported
630 for analysis in MATLAB.

631 For analysis of FtsZ ring dynamics over the entire division process, from nascent Z-ring assembly to
632 late constriction (Figure 1), it was necessary to additionally robustly detecting diffuse patchy FtsZ-
633 rings. We trained the machine learning segmentation tool Ilastik[12] to detect cell outlines with
634 fluorescence images of cells labelled with FtsZ. For detection of diffuse Z-rings, we applied a large
635 Gaussian blur filter to the images, and then multiplied this by the Ilastik-segmented binary image,
636 which had the effect of separating any overlap of Z-rings between adjacent cells. Intensity threshold-
637 based detection of Z-rings was then performed in MicrobeJ as above.

638 *Quantification of division protein septal localization*

639 Custom MATLAB software was developed to measure the diameters and intensities of Z- and 2B-rings
640 obtained from either MicrobeJ or Ilastik. Each frame of each individual ring was first segmented using
641 a multi-level threshold to distinguish the septum, cytoplasm, and background. The septal axis and the
642 cell axis were identified using the segmented image, and the image was rotated such that pixels were
643 aligned along these axes. Line profiles of Z- and 2B-rings were obtained by averaging pixel values along
644 the septal axis ±2 pixels to reduce noise. Diameter were then obtained by fitting line profiles to a toy
645 model that describes a circle of uniform intensity rotated to be orthogonal to the axis of the imaging
646 plane ('Tilted Circle Model', Supplementary Note 1, Supplementary Figure 26). Septal density was
647 calculated as the total intensity along the lateral line profile, divided by the ring circumference, as
648 calculated from the constriction rated analysis (below) to reduce single frame noise. Septal density
649 was used in place of total intensity, in order to compare to the septal intensity measurements
650 obtained during the VerCINI experiments. Axial thickness was estimated by fitting an axial line profile
651 to an analytical super-Gaussian and calculating the full-width half maximum.

Evaluation of percentage Z-rings condensed and constricted post-treatment

Since PC19 treatment causes bright fluorescent foci to appear randomly throughout the cell in strains where FtsZ is labelled, tracking software fails to consistently follow most Z-rings post-treatment in the SH130 and SH212 strains. Furthermore, measurements of Z-ring thickness and diameter were inaccurate due to the proximity of fluorescent foci. Since it was typically straightforward to observe, whether Z-rings condensed and/or constricted post-PC19 treatment was evaluated manually.

FtsZ filament treadmilling analysis from TIRF microscopy data

Images were denoised and registered as above. TrackMate[49] was used to help identifying treadmilling FtsZ filaments outside of dense Z-rings. A line region of interest (ROI) was drawn perpendicular to the cell axis where treadmilling filaments were identified. Kymographs were calculated along this line profile FtsZ filaments trajectories in the kymograph were marked with a line ROI (Supplementary Figure 22). Treadmilling speed for each filament trajectory was calculated from the angle of the line ROIs.

Constriction rate analysis

Previous models for septal constriction have either been *ad hoc*[26] or tailored to Gram-negative cell division based on remodelling of a hemispherical cap[27]. We derived a simple model for Gram-positive constriction, assuming (i) outside-in synthesis of a flat plate at mid-cell and (ii) total PG synthesis rate around the septal leading edge is constant (Supplementary note 2)

$$d(t) = \begin{cases} d_0, & t < t_0 \\ \sqrt{d_0^2 - \frac{4k}{\pi}(t - t_0)}, & t \geq t_0 \end{cases}$$

Where d_0 is the initial Z- or 2B-ring diameter, t_0 is the time constriction begins, and k is the rate at which area is added to the septal plate. This model fitted measured constriction trajectories well, and the estimated time of constriction completion corresponded closely to completion times independently estimated from PBP2B departure in wild type cells (Supplementary Figure 27).

We measured constriction rates in the mNeonGreen-PBP2B strain, since FtsZ-GFP mislocalises post-treatment with PC19 and makes it difficult to track large numbers of septa. A small amount of mNeonGreen-PBP2B signal remained at mid-cell after constriction had finished. This excess signal was excluded from the rate analysis by cutting the 2B-ring data after this drop in intensity. We obtained constriction time distributions for PC19-treated cells by fitting only to post-treatment data.

For comparison to previous observations we converted the observed constriction rates to an effective constriction time t_{eff}, the total amount of time it would take for an unconstricted septum to constrict completely (Methods) given the fitted rate k : $t_{eff} = 2\pi \cdot \frac{d_0^2}{k}$. The average diameter of the unconstricted septum d_0 was estimated as 1100 ± 100 nm (mean, SD) for the mNeonGreen-PBP2B based on the background fluorescence signal in the cell.

Statistics

Data were analysed using estimation statistics, which focusses on magnitude and robustness of effect size using DABEST[50] (Data Analysis with Bootstrap Coupled Estimation), rather than just statistical significance/ p-value. Averages reported were median values unless otherwise indicated. All effect size estimates were calculated based on difference of medians. 95% confidence interval of the median, or of the difference of medians, was estimated by bootstrapping (https://github.com/HoldenLab/violinplusDABEST-Matlab) and indicated with square brackets [].

692 Interquartile range was indicated by IQR. Thick error bar lines in Violin plots indicate interquartile
693 range, thin lines indicate adjacent vales. Error bars in DABEST plots indicate 95% CI of median
694 difference, estimated by bootstrapping. Sample size, indicating number of filaments/Z-ring, cells,
695 microscope fields of view, technical and biological replicates, as appropriate, is presented for each
696 dataset in Supplementary Table 3.

697 **Simulations of FtsZ filament dynamics**

698 Simulated time lapse movies of FtsZ filament dynamics in vertically immobilized cells were generated.
699 Source code for simulations is available (https://github.com/HoldenLab/ring-simulator). Filament
700 speed and lifetime were sampled from distributions obtained from experiments via bootstrap
701 resampling. FtsZ filament distributions were taken from cells expressing FtsZ-GFP in the nascent Z-ring
702 cell division state. Sub-diffraction-limited treadmilling filaments were simulated on a diffuse Gaussian-
703 Cauchy cytoplasmic background described above. Filament intensity, background amplitude and
704 shape parameters all matched average parameters experimentally observed in nascent Z-rings.
705 Photon noise and manufacturer specified camera gain and read noise were added to the images. The
706 number of filaments in each simulated Z-ring was drawn from a Poisson distribution with average
707 filament density equal to observed nascent, mature, 2x mature or 12x mature Z-ring density of (1.3,
708 3.3, 6.5, 37.5 filaments/ Z-ring/ frame). Filament density of real nascent Z-rings was calculated directly
709 from observed number of manually traced filaments, as the filament density there was low enough
710 that filament detection bias was expected to be low. To minimize possible under-detection bias,
711 filament density in mature Z-rings was estimated by multiplying the estimated nascent Z-ring density
712 by the ratio of total Z-ring intensity for mature and nascent Z-rings (Supplementary Figure 8b).
713 Additional simulations at 2x and 12x mature Z-ring filament densities were performed in order to
714 investigate the extent to which large increases to filament density could perturb observed FtsZ
715 filament speeds. Simulated FtsZ ring time lapse movies were analysed identically to the experimental
716 data, with FtsZ filament speed estimated by kymograph analysis. Increased FtsZ filament density
717 caused a decrease in the fraction of detected filaments but had minimal effect on observed FtsZ
718 filament speeds, or the ratio of immobile:treadmilling FtsZ filaments, i.e. the ability to robustly detect
719 both immobile and treadmilling FtsZ filaments (Supplementary Figure 10).

720 **Step finding analysis of Z-ring axial thickness data**

721 Transitions between a decondensed and condensed Z-ring for SH130 cells expressing FtsZ-GFP Z-rings
722 was measured using a step finding algorithm to detect either one or two states in time series Z-ring
723 axial thickness, using a global change point detection algorithm[51] implemented in the MATLAB
724 function *findchangepts().* State detection was performed based on changes in standard deviation of
725 the time series, with an additional threshold that detected axial thickness states should differ by at
726 least 50 nm.

727 **Analysis of Z-ring axial thickness data for FtsZ(D213A) mutant**

728 Although the step-finding method described above accurately located the decondensed-to-
729 condensed transition in wild-type cells, we found that this method was inadequate for the
730 FtsZ(D213A) mutant, as the condensation transition was often slower and more gradual than in wild-
731 type. Instead, Z-rings were considered to have condensed if the thickness dropped below a threshold
732 value for at least one frame (1 min) prior to the start of constriction. The threshold was chosen as 1σ
733 above the mean thickness for condensed wild-type cells (356 nm; Supplementary Figure 17).

DATA AVAILABILITY

Source data for all figures presented in the paper and Supplementary Information, as well as raw movie files for all Supplementary Videos are available at

https://data.ncl.ac.uk/projects/FtsZ_treadmilling_is_essential_for_Z-ring_condensation_and_septal_constriction_initiation_in_Bacillus_subtilis_cell_division/92465

CODE AVAILABILITY

Custom software is available on the Holden lab GitHub page:

https://github.com/HoldenLab/Ring_Analysis_IJ
https://github.com/HoldenLab/ring-fitting2
https://github.com/HoldenLab/DeepAutoFocus
https://github.com/HoldenLab/ring-simulator

746 **REFERENCES**

747 1. Bisson-Filho, A. W. *et al.* Treadmilling by FtsZ filaments drives peptidoglycan synthesis and
748 bacterial cell division. *Science* **355**, 739–743 (2017).
749 2. Yang, X. *et al.* GTPase activity–coupled treadmilling of the bacterial tubulin FtsZ organizes septal
750 cell wall synthesis. *Science* **355**, 744–747 (2017).
751 3. Monteiro, J. M. *et al.* Peptidoglycan synthesis drives an FtsZ-treadmilling-independent step of
752 cytokinesis. *Nature* (2018) doi:10.1038/nature25506.
753 4. Perez, A. J. *et al.* Movement dynamics of divisome proteins and PBP2x:FtsW in cells of
754 Streptococcus pneumoniae. *Proc. Natl. Acad. Sci.* **116**, 3211–3220 (2019).
755 5. Baranova, N. *et al.* Diffusion and capture permits dynamic coupling between treadmilling FtsZ
756 filaments and cell division proteins. *Nat. Microbiol.* **5**, 407–417 (2020).
757 6. Yao, Q. *et al.* Short FtsZ filaments can drive asymmetric cell envelope constriction at the onset of
758 bacterial cytokinesis. *EMBO J.* e201696235 (2017) doi:10.15252/embj.201696235.
759 7. Strauss, M. P. *et al.* 3D-SIM Super Resolution Microscopy Reveals a Bead-Like Arrangement for
760 FtsZ and the Division Machinery: Implications for Triggering Cytokinesis. *PLoS Biol* **10**, e1001389
761 (2012).
762 8. Holden, S. J. *et al.* High throughput 3D super-resolution microscopy reveals *Caulobacter*
763 *crescentus* in vivo Z-ring organization. *Proc. Natl. Acad. Sci.* **111**, 4566–4571 (2014).
764 9. Loose, M. & Mitchison, T. J. The bacterial cell division proteins FtsA and FtsZ self-organize into
765 dynamic cytoskeletal patterns. *Nat. Cell Biol.* **16**, 38–46 (2014).
766 10. Levin, P. A., Kurtser, I. G. & Grossman, A. D. Identification and characterization of a negative
767 regulator of FtsZ ring formation in Bacillus subtilis. *Proc. Natl. Acad. Sci.* **96**, 9642–9647 (1999).
768 11. Ducret, A., Quardokus, E. M. & Brun, Y. V. MicrobeJ, a tool for high throughput bacterial cell
769 detection and quantitative analysis. *Nat. Microbiol.* **1**, 1–7 (2016).
770 12. Berg, S. *et al.* ilastik: interactive machine learning for (bio)image analysis. *Nat. Methods* **16**, 1226–
771 1232 (2019).

772 13. Monahan, L. G., Robinson, A. & Harry, E. J. Lateral FtsZ association and the assembly of the
773 cytokinetic Z ring in bacteria. *Mol. Microbiol.* **74**, 1004–1017 (2009).
774 14. Erickson, H. P., Anderson, D. E. & Osawa, M. FtsZ in Bacterial Cytokinesis: Cytoskeleton and Force
775 Generator All in One. *Microbiol. Mol. Biol. Rev.* **74**, 504–528 (2010).
776 15. Walker, B. E., Männik, J. & Männik, J. Transient Membrane-Linked FtsZ Assemblies Precede Z-Ring
777 Formation in Escherichia coli. *Curr. Biol.* **30**, 499-508.e6 (2020).
778 16. Ellefsen, K. L., Dynes, J. L. & Parker, I. Spinning-Spot Shadowless TIRF Microscopy. *PLOS ONE* **10**,
779 e0136055 (2015).
780 17. Luisier, F., Vonesch, C., Blu, T. & Unser, M. Fast interscale wavelet denoising of Poisson-corrupted
781 images. *Signal Process.* **90**, 415–427 (2010).
782 18. Haydon, D. J. *et al.* An Inhibitor of FtsZ with Potent and Selective Anti-Staphylococcal Activity.
783 *Science* **321**, 1673–1675 (2008).
784 19. Elsen, N. L. *et al.* Mechanism of action of the cell-division inhibitor PC190723: Modulation of FtsZ
785 assembly cooperativity. *J. Am. Chem. Soc.* **134**, 12342–12345 (2012).
786 20. Wagstaff, J. M. *et al.* A polymerization-associated structural switch in FtsZ that enables
787 treadmilling of model filaments. *mBio* **8**, e00254-17 (2017).
788 21. Artola, M. *et al.* The structural assembly switch of cell division protein FtsZ probed with
789 fluorescent allosteric inhibitors. *Chem. Sci.* **8**, 1525–1534 (2017).
790 22. Adams, D. W., Wu, L. J., Czaplewski, L. G. & Errington, J. Multiple effects of benzamide antibiotics
791 on FtsZ function. *Mol. Microbiol.* **80**, 68–84 (2011).
792 23. Männik, J., Driessen, R., Galajda, P., Keymer, J. E. & Dekker, C. Bacterial growth and motility in
793 sub-micron constrictions. *Proc. Natl. Acad. Sci. U. S. A.* **106**, 14861–14866 (2009).
794 24. Yang, D., Jennings, A. D., Borrego, E., Retterer, S. T. & Männik, J. Analysis of factors limiting
795 bacterial growth in PDMS mother machine devices. *Front. Microbiol.* **9**, (2018).
796 25. McGorty, R., Kamiyama, D. & Huang, B. Active microscope stabilization in three dimensions using
797 image correlation. *Opt. Nanoscopy* **2**, 3 (2013).

798 26. Stokes, N. R. *et al.* Novel inhibitors of bacterial cytokinesis identified by a cell-based antibiotic
799 screening assay. *J. Biol. Chem.* **280**, 39709–39715 (2005).
800 27. Silber, N., Mayer, C., Matos de Opitz, C. L. & Sass, P. Antibiotic-induced degradation of FtsZ reveals
801 distinct stages of Bacillus subtilis FtsZ ring assembly and constriction. *bioRxiv* (2020).
802 28. Lu, C., Stricker, J. & Erickson, H. P. Site-specific mutations of FtsZ - Effects on GTPase and in vitro
803 assembly. *BMC Microbiol.* **1**, (2001).
804 29. Redick, S. D., Stricker, J., Briscoe, G. & Erickson, H. P. Mutants of FtsZ targeting the protofilament
805 interface: Effects on cell division and GTPase activity. *J. Bacteriol.* **187**, 2727–2736 (2005).
806 30. Lyu, Z., Coltharp, C., Yang, X. & Xiao, J. Influence of FtsZ GTPase activity and concentration on
807 nanoscale Z-ring structure in vivo revealed by three-dimensional Superresolution imaging.
808 *Biopolymers* **105**, 725–734 (2016).
809 31. Gamba, P., Veening, J.-W., Saunders, N. J., Hamoen, L. W. & Daniel, R. A. Two-Step Assembly
810 Dynamics of the Bacillus subtilis Divisome. *J. Bacteriol.* **191**, 4186–4194 (2009).
811 32. Grimm, J. B. *et al.* A general method to improve fluorophores for live-cell and single-molecule
812 microscopy. *Nat. Methods* **12**, 244–250 (2015).
813 33. Westfall, C. S. & Levin, P. A. Bacterial Cell Size: Multifactorial and Multifaceted. *Annu. Rev.*
814 *Microbiol.* **71**, 499–517 (2017).
815 34. Dajkovic, A., Pichoff, S., Lutkenhaus, J. & Wirtz, D. Cross-linking FtsZ polymers into coherent Z
816 rings. *Mol. Microbiol.* **78**, 651–668 (2010).
817 35. Caldas, P. *et al.* Cooperative ordering of treadmilling filaments in cytoskeletal networks of FtsZ
818 and its crosslinker ZapA. *Nat. Commun.* **10**, 5744 (2019).
819 36. Huecas, S. *et al.* Self-Organization of FtsZ Polymers in Solution Reveals Spacer Role of the
820 Disordered C-Terminal Tail. *Biophys. J.* **113**, 1831–1844 (2017).
821 37. Sundararajan, K. & Goley, E. D. The intrinsically disordered C-terminal linker of FtsZ regulates
822 protofilament dynamics and superstructure in vitro. *J. Biol. Chem.* **292**, 20509–20527 (2017).

823 38. Buske, P. J. & Levin, P. A. A flexible C-terminal linker is required for proper FtsZ assembly in vitro
824 and cytokinetic ring formation in vivo. *Mol. Microbiol.* **89**, 249–263 (2013).
825 39. Denk, J., Huber, L., Reithmann, E. & Frey, E. Active Curved Polymers Form Vortex Patterns on
826 Membranes. *Phys. Rev. Lett.* **116**, 178301 (2016).
827 40. Pasquina-Lemonche, L. *et al.* The architecture of the Gram-positive bacterial cell wall. *Nature* **582**,
828 294–297 (2020).
829 41. Coltharp, C., Buss, J., Plumer, T. M. & Xiao, J. Defining the rate-limiting processes of bacterial
830 cytokinesis. *Proc. Natl. Acad. Sci.* 201514296 (2016) doi:10.1073/pnas.1514296113.
831 42. de Jong, I. G., Beilharz, K., Kuipers, O. P. & Veening, J.-W. Live Cell Imaging of Bacillus subtilis and
832 Streptococcus pneumoniae using Automated Time-lapse Microscopy. *J. Vis. Exp.* (2011)
833 doi:10.3791/3145.
834 43. Harwood, C. R. & Cutting, S. M. *Molecular biological methods for Bacillus*. (Wiley, 1990).
835 44. Koo, B.-M. *et al.* Construction and Analysis of Two Genome-Scale Deletion Libraries for Bacillus
836 subtilis. *Cell Syst.* **4**, 291-305.e7 (2017).
837 45. Ellefsen, K. L., Dynes, J. L. & Parker, I. Spinning-Spot Shadowless TIRF Microscopy. *PLOS ONE* **10**,
838 e0136055 (2015).
839 46. Thevenaz, P., Ruttimann, U. E. & Unser, M. A pyramid approach to subpixel registration based on
840 intensity. *IEEE Trans. Image Process.* **7**, 27–41 (1998).
841 47. Dos Santos Caldas, P. R., Radler, P., Sommer, C. M. & Loose, M. Computational analysis of filament
842 polymerization dynamics in cytoskeletal networks. *Methods Cell Biol.* (2020).
843 48. Eberly, D., Gardner, R., Morse, B., Pizer, S. & Scharlach, C. Ridges for image analysis. *J. Math.*
844 *Imaging Vis.* **4**, 353–373 (1994).
845 49. Tinevez, J.-Y. *et al.* TrackMate: An open and extensible platform for single-particle tracking.
846 *Methods* **115**, 80–90 (2017).
847 50. Ho, J., Tumkaya, T., Aryal, S., Choi, H. & Claridge-Chang, A. Moving beyond P values: data analysis
848 with estimation graphics. *Nat. Methods* **16**, 565–566 (2019).

51. Killick, R., Fearnhead, P. & Eckley, I. A. Optimal Detection of Changepoints With a Linear Computational Cost. *J. Am. Stat. Assoc.* **107**, 1590–1598 (2012).